Flow Separation Control with Rotating Cylinders

by

James Crandall Schulmeister

B.S., Yale University (2008)

Submitted to the Department of Mechanical Engineering
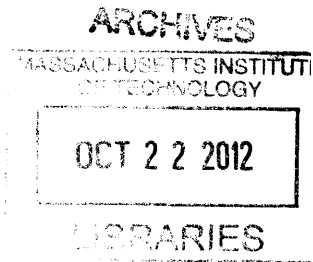in partial fulfillment of the requirements for the degree of

Master of Science in Ocean Engineering

at the

MASSACHUSETTS INSTITUTE OF TECHNOLOGY

September 2012

Author . . . .
Department of Mechanical Engineering
August 10, 2012

Certified by . . . .
Michael S Triantafyllou
Professor of Mechanical and Ocean Engineering
Thesis Supervisor

Accepted by . . . .
David E Hardt, Professor of Mechanical Engineering
Chairman, Department Committee on Graduate Theses

Flow Separation Control with Rotating Cylinders

by

James Crandall Schulmeister

Abstract

The hydrodynamic forces on ocean vehicles increase dramatically during sharp maneuvers as compared to forward motion due to large areas of separated flow. These large forces severely limit maneuverability and reduce efficiency. Applying active flow separation control to ocean vehicles would reduce resistance during maneuvers and thereby improve maneuvering performance.

In this thesis I discuss experiments in active separation control in a simpler, but still relevant, two-dimensional flow past a circular cylinder at moderate sub-critical Reynolds numbers (37,000 and 52,000 in experiment and 100 and 10,000 in simulation). The active control injects momentum into the boundary layer via the moving surfaces of two small control cylinders located near boundary layer separation and rotated by servo motors. The relationship between drag and rotation rate is found to be Reynolds number regime dependent; at Re = 100 the drag decreases linearly with rotation rate and at Re = 10,000, the relationship is non-linear. This non-linearity appears to be due to the interaction between vortex shedding from the small control cylinders (which does not occur at Re = 100) and the main cylinder wake. Computational two-dimensional viscous simulations are consistent with the physical experiment and help to illustrate the phenomenon. Finally, the power consumed by the active control mechanism is considered and estimated to be significantly smaller than the power savings in reduced drag.

Thesis Supervisor: Michael S Triantafyllou
Title: Professor of Mechanical and Ocean Engineering

Acknowledgments

I first want to acknowledge my advisor, Professor Michael S. Triantafyllou, and Dr. Jason Dahl. Their insight, guidance, and patience were invaluable throughout the past two years. Past and current members of the MIT Towing Tank Lab, Vicente Fernandez, Audrey Maertens, Jeff Dusek, Heather Beem, Stephanie Steele, Amy Gao, and Jacob Izraelevitz provided great technical feedback and support. Gabe Weymouth created the open source Lily Pad code and has been very helpful in answering any questions I have. Special thanks goes to Maha Haji for her help developing the experimental setup. And finally, I want to thank my family and friends for their support.

Contents

List of Figures

10

List of Tables

Chapter 1

Introduction

1.1 Motivation

Ocean vehicles are generally designed to be as streamlined as possible to minimize resistance as they move through water, subject to other design constraints. While streamlined shapes reduce form drag in their forward direction, vehicles frequently encounter flows at significant angles of attack to the forward direction during maneuvers. When moving at an angle of attack, streamlined shapes are no longer streamlined and suffer the same flow separation and resulting dramatic increases in hydrodynamic forcing as bluff shapes. As a result, streamlined vehicles must overcome very large resistance to maintain speed during maneuvers. In water tunnel experiments, Han and Patel were able to visualize vortex separation on a streamlined axisymmetric body at an angle of attack (figure 1-1)[7]. This vortex separation has also been successfully captured by three-dimensional viscous simulations (figure 1-2).

Maneuverability can be improved by one of two strategies or a combination of the two. The first is to increase the force that a vehicle can exert on the water. The second is to reduce the resistance to maneuvering, the dominant cause of which is flow separation. In this thesis I investigate the second of these for the flow past a circular cylinder. Small rotating cylinders inject momentum into the slow-moving boundary layer flow to delay separation and reduce drag. Flow separation for a circular cylinder is much simpler than that for a typical ocean vehicle because it is predominantly two-
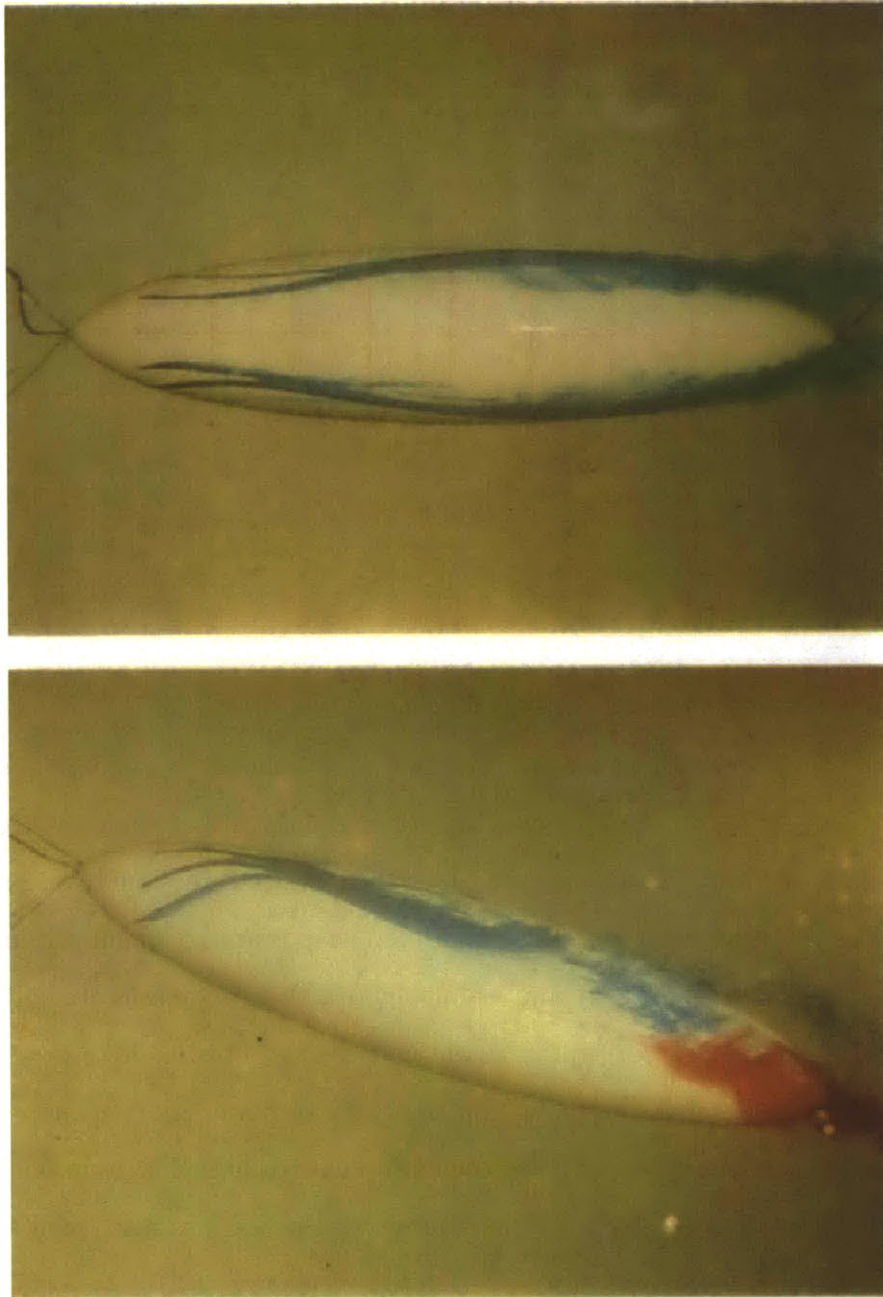
Figure 1-1: Adapted from [7], dye visualization of vortex separation on a 6:1 prolate spheroid in a flow of 20° incidence to the axis of rotational symmetry.

dimensional. However, similar physics apply to the cylinder so it is a sensible first step in designing a mechanism that will someday effectively control three dimensional flow separation on maneuvering ocean vehicles.

Figure 1-2: Simulated vortex separation from a canonical submersible shape in a flow of 30° incidence to the axis of rotational symmetry. Courtesy of Dr. Gabriel Weymouth.

1.2 Chapter Preview

Chapter two provides background information on flow separation control techniques and in particular a review of the literature on flow separation control with rotating cylinders.

Chapter three describes the design, implementation, and results from a physical experiment in rotating cylinder separation control for the flow past a circular cylinder. The experiment was conducted in the MIT Water Tunnel at Reynolds number 37,000 and 52,000. Forces were measured with a six-axis strain gauge and the mean flow was measured with the Laser Doppler Anemometry technique.

Chapter four describes two-dimensional computational simulations of the same, which were conducted with the open-source solver, Lily Pad. Simulations were conducted at Reynolds number 100 and 10,000.

Chapter four compares the results of the physical and computational experiments, discusses Reynolds number effects, and considers the power consumption of the control mechanism.

Chapter five presents conclusions and a discussion of appropriate future work on this topic.

Chapter 2

Background

2.1 Flow Separation

Flow separation is a phenomenon in which a streamline radiates from a submerged solid surface. In attached flows, the streamlines nearest a solid surface are instead everywhere parallel to the surface. Flow separation arises from the combination of a slow moving boundary layer with an adverse pressure gradient. The slow-moving boundary layer is created by the viscosity of the fluid itself when it flows over submerged solid surfaces, which have no-slip surface condition. Adverse pressure gradients are created when a body of finite dimensions moves through a fluid; fluid particles are first forced to accelerate out of the way of the body via a favorable pressure gradient and then to decelerate to their initial condition at rest via an adverse pressure gradient. In separated flow, the pressure in the fluid downstream of the separation point is much lower than it would be for an attached flow, which causes a large increase to the drag [18].

2.2 Relevant non-dimensional parameters

The Reynolds number expresses the relative importance of inertial and viscous forces in a flow. Inertial forces are more important in high Reynolds number flows and viscous forces are more important in low Reynolds number flows. The boundary
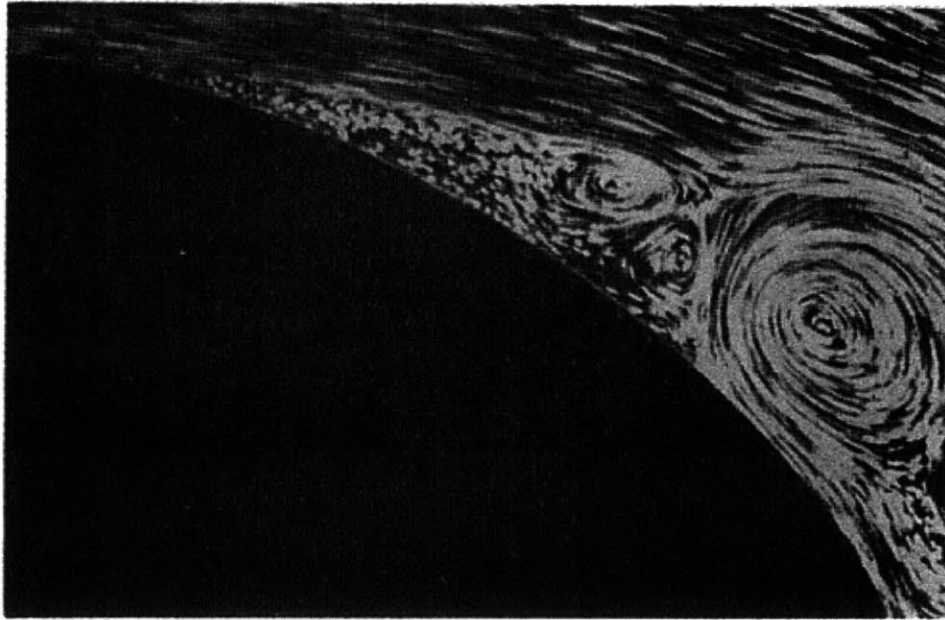
Figure 2-1: Adapted from [18]. The boundary layer separates in the adverse pressure gradient on the downstream side of a bluff body.

layer is the region of the flow close to submerged solid surfaces in which viscous forces dominate.

$$Re = \frac{DU}{\nu}$$

Separated flows are often accompanied by unsteady vortex shedding. The Strouhal number is the reduced frequency of vortex shedding.

$$Str = \frac{fD}{U}$$

Drag and lift forces are generally non-dimensionalized as coefficients of lift and drag, C_L and C_D, by the stagnation pressure and cross-sectional area.

$$C_L = \frac{Lift}{\frac{1}{2}\rho U^2 A}$$

$$C_D = \frac{Drag}{\frac{1}{2}\rho U^2 A}$$

In this thesis, it is convenient to normalize the forces by their value with zero control effort so that the effect of flow control is immediately apparent. The rotation parameter, ξ, represents control effort and is defined in the next section.

$$C_L(\xi) = \frac{Lift(\xi)}{Lift|_{\xi=0}}$$

$$C_D(\xi) = \frac{Drag(\xi)}{Drag|_{\xi=0}}$$

2.3 Flow Separation Control

Flow separation results in large hydrodynamic forces that can limit performance and even be desctructive to engineered structures like airplanes, ships, submarines, buildings, bridges, etc. Flow separation control refers to any effort to control the location on a body where flow separates. In general, delaying separation to locations further downstream from the uncontrolled state reduce both the mean and fluctuating hydrodynamic forces.

2.3.1 Passive Control

Passive control strategies are those that do not require power input. Passive control mechanisms largerly include small changes to the geometry of a body that trigger a transition to turbulent flow in the boundary layer. Turbulence in a boundary layer transports momentum normal to the mean flow direction, which helps flow to stay attached in the presence of an adverse pressure gradient. As a result, turbulent boundary layers separate at greater adverse pressure gradients than laminar boundary layers [6].

2.3.2 Active Control

Active control strategies, as compared to passive strategies, do require power input. Active strategies are particularly useful in applications where flow conditions change

dramatically and rapidly. Active mechanisms can be implemented with close-loop feedback control of actuation to react to changing flow conditions [6].

Active mechanisms generally take the form of suction, jets, or moving surfaces. These can be designed with either zero or non-zero net mass flux. Zero net mass flux designs are more applicable to external flows, such as the flow past a marine vehicle.

2.3.3 Rotating Cylinder Flow Separation Control

Rotating cylinder control is an active separation control strategy that uses the moving surface of a rotating circular cylinder. It is an active mechanism because the rotation of the cylinders requires power input. It is a zero net mass flux mechanism because fluid does not pass through any of the surfaces. The level of control effort is measured by the rotation parameter. The rotation parameter, ξ, is the surface speed of the rotating cylinder normalized by the free stream velocity.

$$\xi = \frac{u_{surface}}{u_\infty}$$

The moving surface of a rotating cylinder injects momentum into its boundary layer flow via the no-slip condition at its surface. The flow past a single circular cylinder rotating at a constant rate can generate lift coefficients greater than 20 and complete suppression of vortex shedding [1]. Drag reduction and suppression of vortex shedding have also been accomplished through rotary oscillation [8].

Rotating cylinder control can also be implemented with multiple bodies. Most commonly, the rotating cylinder is smaller than the primary body and can be located in the immediate vicinity of the primary body or even immersed in the primary body with only a fraction exposed to the external flow. Modi discusses the various arrangements in which rotating cylinders have been used in his review of moving surface boundary layer control [11]. His review focused on works that used rotating cylinders in thin airfoils and at the sharp corners of angled bluff bodies. He discusses experiments and simulations completed at Reynolds numbers up to $4\text{x}10^4$. In many cases, cylinders inset in larger bodies and partially exposed to the flow while rotating

with $\xi > 1$ provide increased lift and decreased drag. Some arrangements of cylinders applied to an airfoil are shown in figure 2-2.
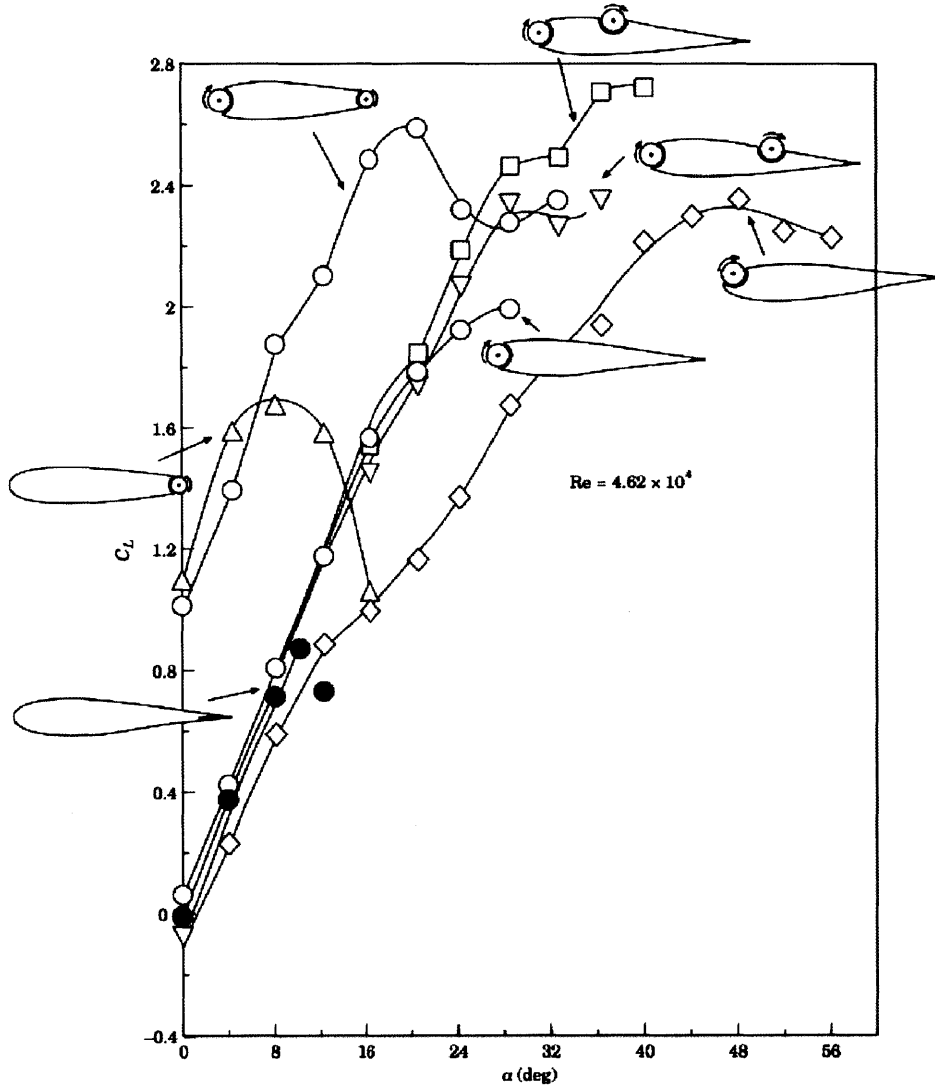
Figure 2-2: Adapted from [11]. Rotating cylinder separation control applied to airfoils with $\xi = 4$ for all rotating cylinders.

In arrangements in which the small control cylinders are completely external to the primary body, the presence of the control cylinders by itself can significantly alter the wake without rotating. Kuo et al find that locating two small cylinders in the wake of a larger main circular cylinder can passively reduce form drag as well as fluctuating lift and drag [9].

Mittal investigates in [10] the control of flow past a circular cylinder with small

rotating control cylinders located completely external to the main cylinder, shown in figure 2-3. Mittal investigates the effect of the gap width on drag reduction and finds that there is a critical gap width beyond which greater rotation rate achieves negligible drag reduction. Muddada and Patnaik investigate external rotating control cylinders located at 120° to the upstream stagnation point, shown in figure 2-4.
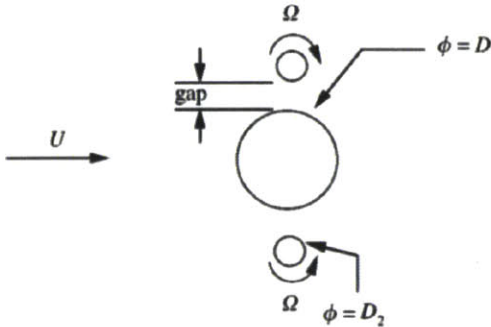
Figure 2-3: Adapted from [10]. Diagram of rotating cylinder flow control with external rotating control cylinders.
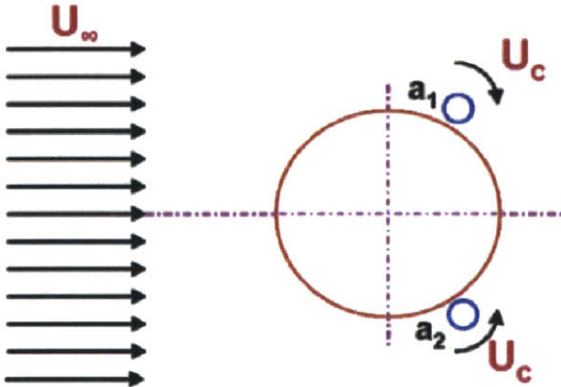
Figure 2-4: Adapted from [12]. Diagram of rotating cylinder flow control with external rotating control cylinders.

In addition to purely hydrodynamics investigations, simulations of feedback control of the cylinder rotation rate is investigated in [14], [2], [12], and [3].

Chapter 3

Physical Experiment

3.1 Experiment Description

Separated flow past a maneuvering streamlined vehicle shape is highly three-dimensional. However, the predominantly two-dimensional flow past a circular cylinder exacerbates flow separation and can be considered a worst-case scenario in which a streamlined vehicle encounters flow broad side. It was therefore selected for this investigation being relevant and also experimentally convenient. A schematic of the experiment arrangement is provided in figure 3-1.
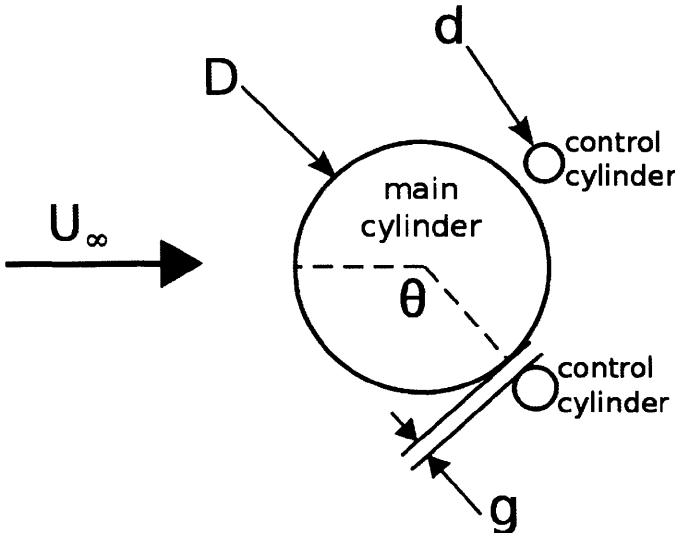
Figure 3-1: Diagram of rotating cylinder control of flow past a circular cylinder

	Re_D	$\frac{d}{D}$	Re_d	$\frac{g}{D}$	ξ	Re_g	θ
Muddada and Patnaik, 2009 (simulation)	100	0.1	10	0.01	< 3	< 1	120°
Mittal, 2001 (simulation)	10,000	0.05	500	0.01	< 6	< 600	90°
Schulmeister, 2012 (experiment)	52,000	0.125	6,500	0.025	< 2	< 3250	120°

Table 3.1: Summary of parameters for the experiment described in this thesis and two similar studies in the literature [12] [10].

The geometry is described by three parameters: $\frac{d}{D}$, $\frac{g}{D}$, and θ. The flow regime requires two additional parameters: Re_D and ξ. All five of these parameters are necessary to completely describe the flow. It is equivalent and useful to use Re_d and Re_g, defined below, in place of the length ratios.

$$Re_d = \frac{d}{D} Re_D$$

$$Re_g = \frac{g}{D} \xi Re_D$$

The most important variation between these studies is the Reynolds number (Re) because vortex shedding modes vary with Re. In particular, vortex shedding occurs in steady flows past circular cylinders for Re greater than 40 [22]. While vortex shedding is expected from the main cylinder in all studies, vortex shedding from the smaller control cylinders is expected only in Mittal's simulation and this experiment.

The effect of vortex shedding from the smaller control cylinders on the large scale wake will be a function of the relative strength, size, and frequency of shed vortices. All of these scale with diameter, so the ratio, $\frac{d}{D}$, indicates the relative importance of vortex shedding from the control and main cylinders. As a result, the influence of vortex shedding from the control cylinders is most pronounced in this experiment.

3.2 Experiment Apparatus

An apparatus that implements rotating cylinder control for the flow past a circular cylinder in the MIT water tunnel was designed and fabricated to carry out the experiments discussed in this thesis. The goal was to implement rotating cylinder control of the flow past a circular cylinder at higher Reynolds numbers than have been investigated up until now. The final apparatus reached Reynolds numbers of 52,000, which is sub-critical but greater than any similar study. The design balanced flow and structural constraints to yield the most accurate and useful results.

3.2.1 Finite End Effects

The geometry under consideration is two-dimensional, so it was important to design the model to mitigate three-dimensional effects that arise from the cylinder's finite length. This can be done with one or both of two strategies. The first is to use a high aspect ratio cylinder so that end effects are confined to a small fraction of the span. The second is to use end plates that prevent the flow from moving perpendicular to the cylinder cross-section plane at the ends [17]. This experiment setup utilizes both of these strategies.

The circular cylinder extends from the top to the bottom of the water tunnel test section with a gap between the test section walls and cylinder ends equal to D/16, (Figure 3-2). The test section walls thus become end plates. The aspect ratio was set to 10, the highest possible without creating significant structural difficulties.

3.2.2 Test Section Blockage

Results obtained in water tunnels do not match results in larger bodies of water because the proximity to test section walls influences the flow. The blockage ratio, which is the ratio between the cross-sectional areas of the model and the test section, is a good measure of the magnitude of blockage effects. Blockage effects become noticeable at ratios greater than 6% [19], but do not appreciably alter measured drag coefficients for ratios less than 10% [22] [16]. The aspect ratio of 10 in this experiment

27
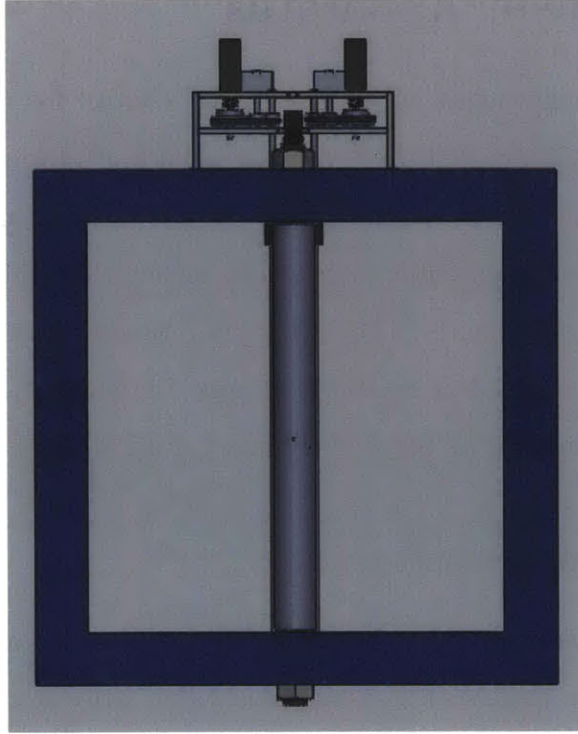
Figure 3-2: Stream-wise view of experiment solid model. The aspect ratio of the cylinder is 10 and the blockage ratio is 10%.

results in a blockage ratio of 10% (Figure 3-2). The importance of a small blockage ratio was balanced by structural difficulties in fabricating small components that rotate at high velocities.

3.2.3 Vibrations

Vibrations are important to consider in the design of dynamic systems. The control cylinders are rotated at high speeds in this experiment to achieve effective flow separation control. As a shaft rotates, small eccentricity in the shaft or bearings exert periodic forcing at as low a frequency as once per revolution. Large amplitude vibrations occur when the forcing frequency matches the frequency of a shaft vibration mode. The lowest critical shaft speed is that which equals the lowest vibration mode frequency and can be estimated with classical linear beam theory [4].

$$\omega_{crit} = (\frac{\pi}{l})^2 \sqrt{\frac{EI}{m}}$$

28

The critical rotation rate for the rotating control cylinders in this experiment was calculated with the above formula. This critical rotation rate must be avoided so that large amplitude vibrations do not occur.

$$\omega_{crit}(control cylinder) = 300.5\frac{rad}{s} \approx 48Hz$$

In addition to rotation of the shaft, the fluid flow also contributes periodic forcing. As vortices shed from a body, the body experiences forcing at the frequency of vortex shedding. The reduced frequency of vortex shedding for a stationary isolated cylinder at moderate sub-critical Reynolds numbers is well known to be $\frac{fD}{U} \approx 0.2$. Although the frequency of vortex shedding from the control cylinders from this experiment will change due to the presence of the larger cylinder, this estimate gives a good approximation of the frequency of fluid forcing. The diameter of the cylinder being fixed, the frequency of vortex shedding is directly proportional to the free stream velocity as shown in figure 3-3. The plot shows the maximum rated rotation rate of the servo motors as well as the fundamental frequency of the control cylinders. The fluid forcing and vibration frequency match at a Reynolds number of 80,000. The experiment should therefore be conducted at significantly lower or greater free stream velocities to avoid large amplitude vibrations. At higher free stream velocities, the maximum achievable rotation parameter, ξ, falls to about 1, which the literature suggests is too low to fully control the flow [11]. The experiment was therefore operated at free stream velocities corresponding to Re < 52,000, which mitigates large amplitude vibrations and permits rotation parameters greater than 1.

The range of rotation rates required to span ξ from 0.0 to 2.0 includes the critical rotation rate of the control cylinders. Figure 3-4 shows how the rotation parameter in the vicinity of the critical rotation rate varies with the free stream velocity. The experiment was conducted at two different free stream velocities, corresponding to Reynolds numbers of 37,000 and 52,000, to avoid the critical rotation rate of the control cylinders. Figure 3-4 shows how experiments at these two Reynolds numbers combine to span the rotation parameter from 0.0 to 2.0 without overlapping the
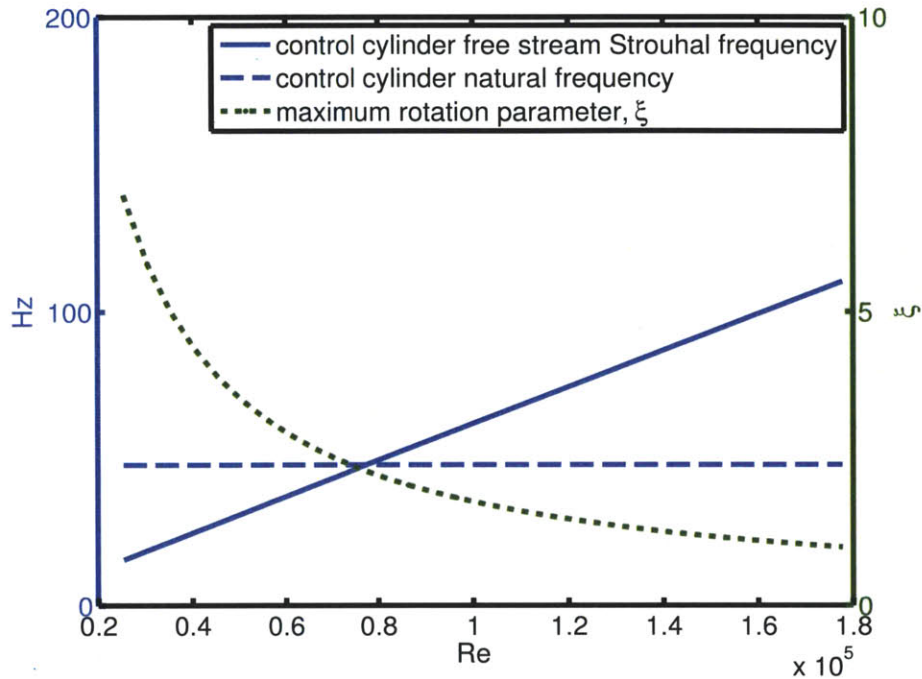
Figure 3-3: Large amplitude vibrations of the control cylinders result when the forcing frequency from vortex shedding matches the first structural vibration mode natural frequency. Additionally, the maximum attainable rotation parameter, ξ, decreases with increasing free stream velocity.

critical rotation rate.

3.2.4   Rotating Cylinders

The control cylinders are rotated with two independent Sigma MM servo motors made by Yaskawa. The servo-motors have a rated maximum continuous rotation rate of 3,000 rpm, which is significantly less than the rotation rate required at the control cylinders. The rotation rate at the cylinder is amplified by 3 with toothed timing belt pulleys. The design also includes an adjustable tensioning pulley to accomodate quick assembly and disassembly, shown in figure 3-5.

The high speed shafts penetrate the window into the test section through teflon bushings. On the test section side of the window, the high speed shafts are co-axially coupled to the control cylinders with a flexure coupling. The flexure coupling is cylindrical with helical cuts that allow the coupling to accomodate some axial and angular misalignment. The control cylinders extend from the flexure coupling at the
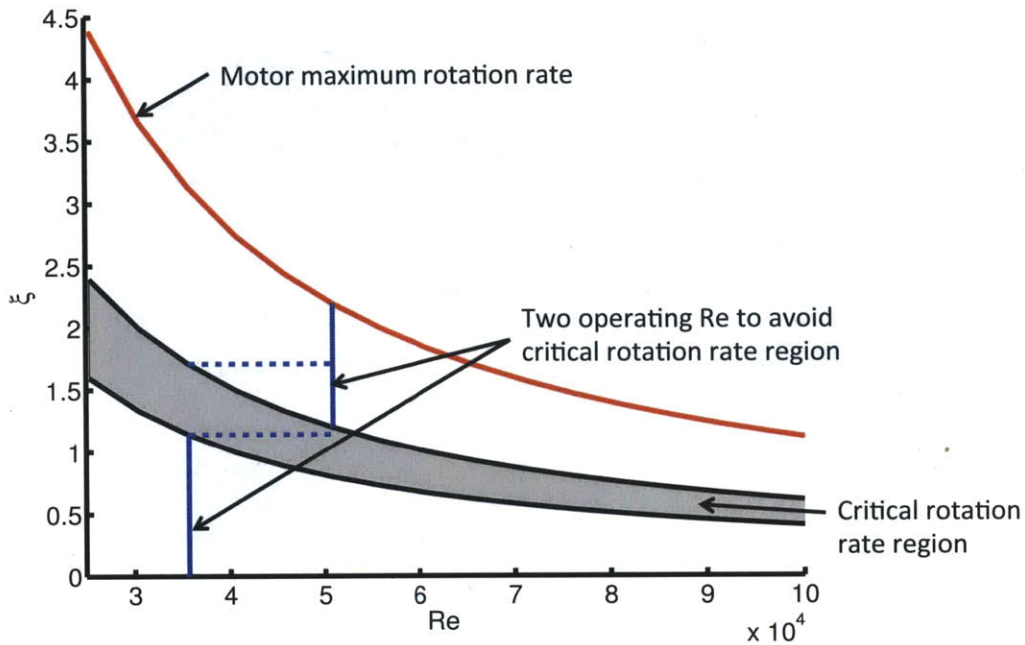
Figure 3-4: The critical shaft rotation rate, which can result in large amplitude vibrations, corresponds to a different range of the rotation parameter at different Reynolds numbers.

top of the test section and terminate at teflon bushings press-fit into the bottom of the test section, shown in figure 3-7.

3.2.5 Measuring Forces

Forces were measured with a 6-axis strain gauge based force sensor manufactured by AMTI Force and Motion (MC-1.0, Figure 3-6). The forces on the entire system, which includes forces on the main cylinder and two small control cylinders, is of interest. However, it was much simpler to mount only the main cylinder on the force transducer. The force transducer therefore measures the forces and moments on the main cylinder, but not the small control cylinders. This is acceptable for two reasons: first, the measured forces on the main cylinder likely dominate the forces on the

31
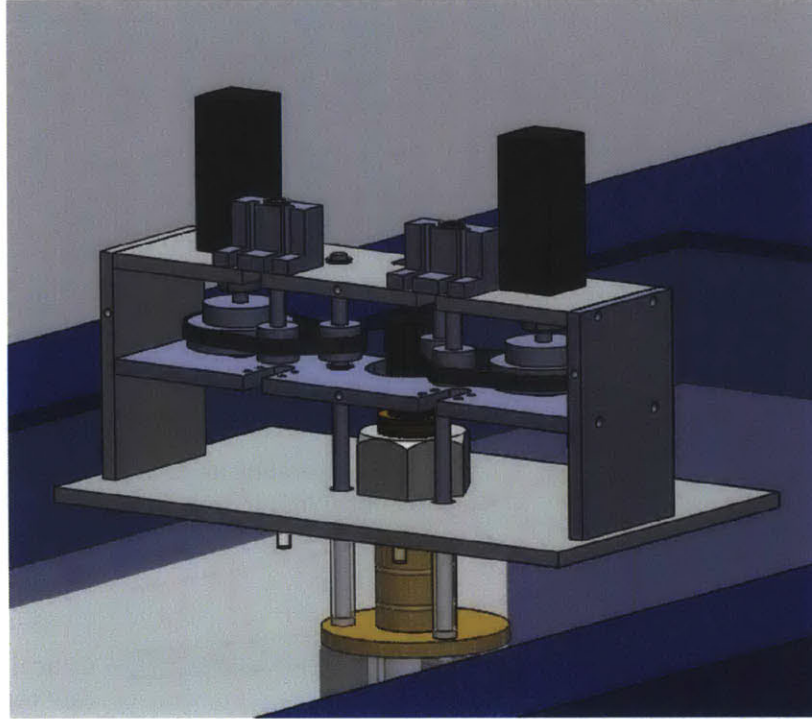
Figure 3-5: Solid model of experiment super-structure that rotates the control cylinders.

combined system and second, mean forces on the combined system can be calculated from mean flow measurements. The force transducer measurements are valuable in addition to mean flow measurements because they can be sampled at a high rate to provide frequency content of the forces, which cannot be accessed from the mean flow field.

The main cylinder was fixed to the force transducer from the inside at the center of its span to avoid exerting large moments on the transducer. The transducer was mounted on an aluminum sting that extends from the top of the test section through the main cylinder. This arrangement is shown in figure 3-7.

3.2.6 Measuring the Flow Field

A Laser Doppler Anemometry (LDA) system from Dantec Dynamics was used to measure the mean flow field. Two lasers are focused at a fixed focal distance from the transmitting optics. In the intersection volume of the two lasers, a fringe pattern of

Figure 3-6: The AMTI MC-1.0 6-axis water-proof force transducer, image from amti.uk.com.
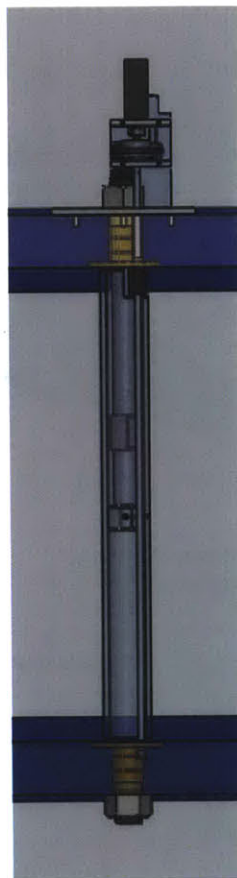
Figure 3-7: The AMTI MC-1.0 force transducer is mouned on a sting that extends from the top of the test section to the mid-span of the main cylinder.

parallel bands of high and low intensity light is formed. As a seeding particle passes through the fringe pattern with band spacing, d_f, the light it reflects is modulated

by the fringes at a frequency equal to the ratio between the particle velocity perpendicular to the fringes and the known fringe wavelength. The frequency, f_b , at which signal bursts, each corresponding to a single particle passing through the intersection volume, are modulated is measured. The particle's velocity projected onto the direction perpendicular to the fringe pattern is calculated as:

$$u = f_b d_f$$

Adding additional laser pairs that share an intersection volume with the first pair and with fringe patterns oriented in different directions enables additional velocity components to be measured. In this experiment, four lasers were used to measure two-dimensional velocity vectors in the plane perpendicular to the cylinder axis.
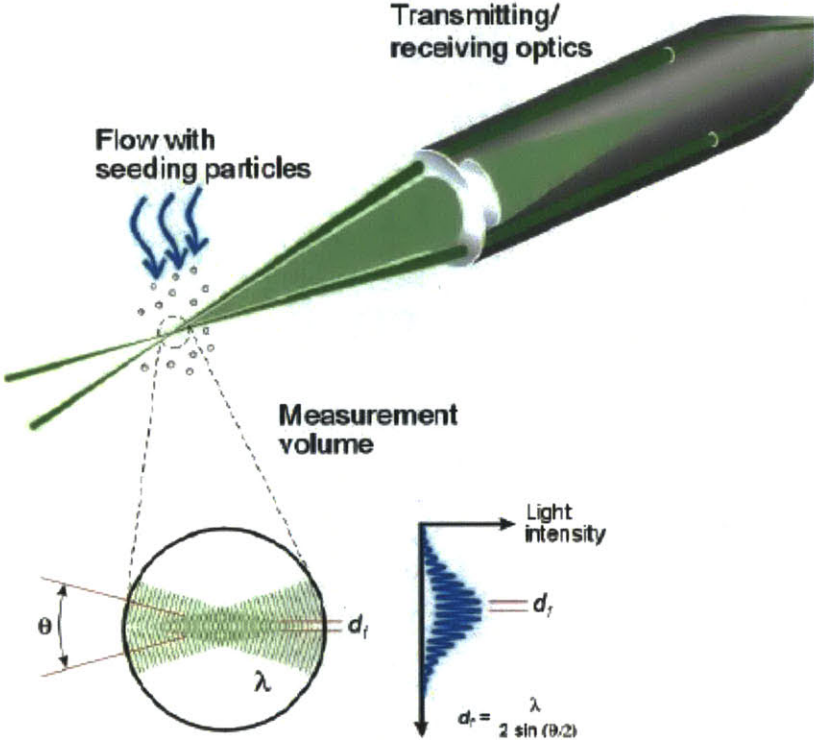
Figure 3-8: Image from Dantec.com illustrates the laser doppler anemometry flow measuring technique.

Flow velocity was measured at an upstream station and in a 100 point rectangular grid in the wake of the cylinder. Line-of-sight obstructions prevented measuring

the flow velocity in the near wake at x/D less than 1.5. The measurement locations relative to the model are shown in figure 3-9. The mean flow field was assembled by collecting 100 velocity readings at each point. The rate at which velocity measurements are made at a single point depends on the power of the laser, the reflectivity of the tracer particles, the distance the lasers must penetrate into the test section, etc. In these experiments, the average data rate was 1Hz, which is too low to glean frequency content. However, the root mean square of the 100 samples at each station does provide some measure of the intensity and area of velocity fluctuations due to vortex shedding. Each velocity measurement was weighted equally in the calculation of the root mean square velocity fluctuation.

$$u_{RMS} = \frac{1}{N}\Sigma_{i=1}^{N}[(u_i - \overline{u})^2]$$
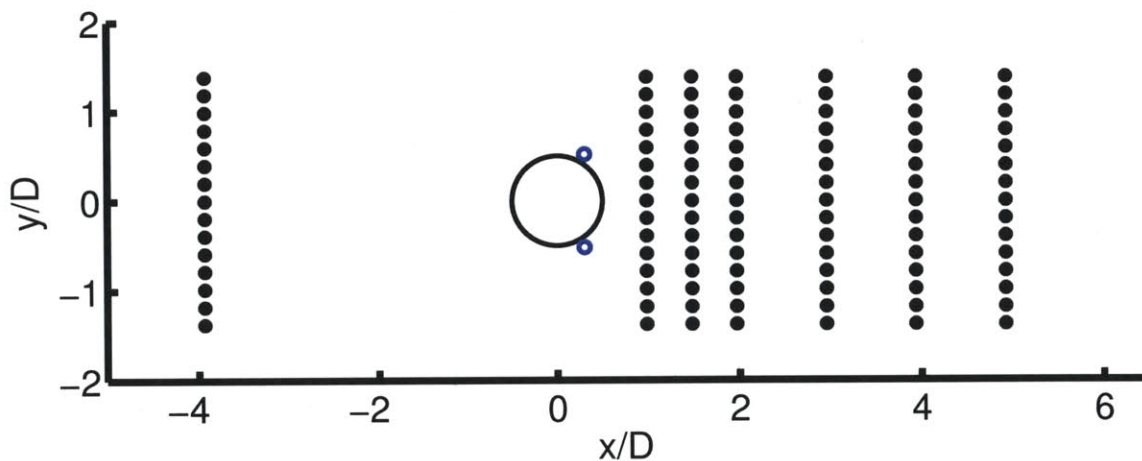
Figure 3-9: Mean velocity measurement locations. Flow is from left to right.

3.3 Force Measurements

3.3.1 Mean Drag

The mean drag coefficient is plotted against the rotation parameter in figure 3-10. In this plot, the drag coefficient is equal to the drag force normalized by its value

with zero control effort. Each data point is the time average of 100 seconds of force measurements sampled at 50,000 Hz. The data was sampled at such a high frequency to prevent aliasing due to high frequency noise introduced by the motors. Since the frequency of vortex shedding was on the order of 3Hz, the 100 second sample time included approximately 300 vortex shedding cycles.

$$C_D = \frac{Drag}{Drag|_{\xi=0}}$$

The drag coefficient is, by definition, equal to 1 with zero control effort. For rotation parameters, ξ, between 0 and 1, the drag inreases by approximately 5%. Drag decreases sharply for ξ between 1 and 1.5 and levels out to a minimum value of approximately 0.8 for ξ greater than 1.5.
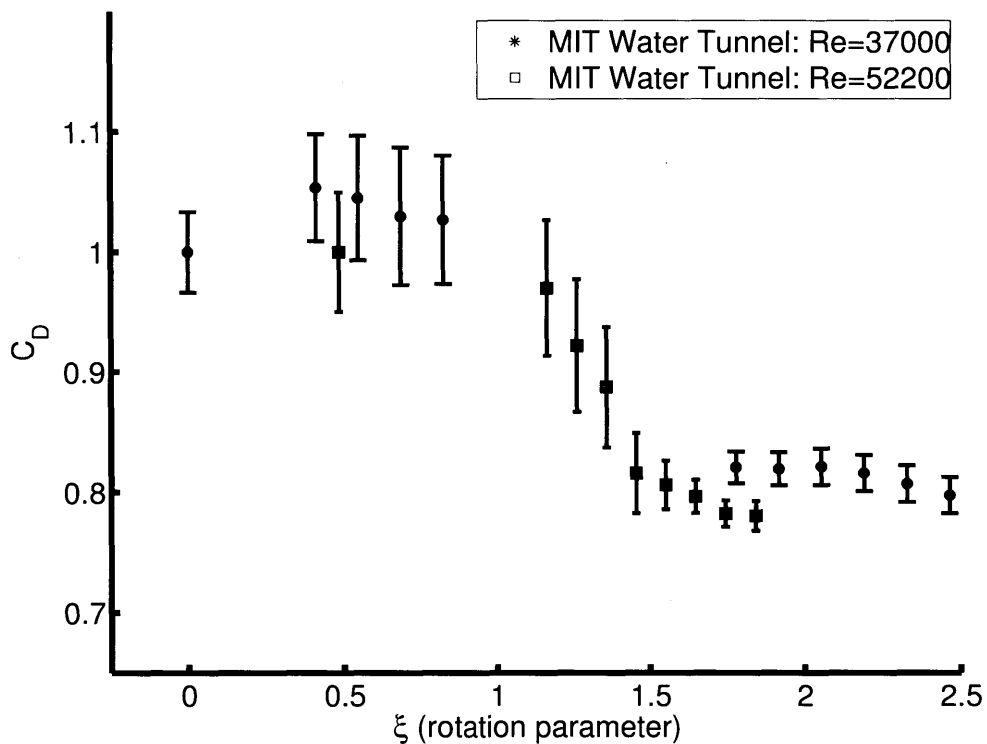
Figure 3-10: Mean drag coefficient: $C_D = \frac{Drag}{Drag|_{\xi=0}}$

The error bars attached to the measured drag coefficients in figure 3-10 represent the standard deviation of drag coefficient fluctuations at frequencies lower than the

vortex shedding frequency. That is, the error bars represent the variation of the mean drag over a vortex shedding period as opposed to variation of the instantaneous drag, which is dominated by vortex shedding. The error bars were calculated by first reducing the sampling frequency with the "decimate" function in MATLAB ®. This function applies an 8th order zero-phase change Chebyshev type 1 filter and then re-samples the filtered data at a lower frequency. This was done twice, first to reduce the size of the data set by a factor of 10 and then by 5. The resulting data set had a sampling frequency of 1,000 Hz, which still captures vortex shedding on the order of 3 Hz very well. The data set was then put through a median filter with bin width equal to a vortex shedding period to remove variation due to vortex shedding. The error bars indicate the standard deviation of this median-filtered signal.

3.3.2 Fluctuating Forces

The mean and fluctuating flows and forces are strongly coupled for the flow past a circular cylinder. The mean drag force is dominated by flow separation and periodically shedding vortices create unsteady forces. The free shear layers created by separation are unstable and roll up into vortices that form the von Karman vortex street and the unsteady forces. Thus, as flow separation and vortex shedding are strongly coupled, so too are the mean and fluctuating forces on a cylinder in cross-flow.

The lift force on the a circular cylinder in a cross flow fluctuates at a reduced frequency $\frac{fd}{u_\infty}$ of approximately 0.2 at the Reynolds numbers on the order of 10,000 [21]. The frequency spectra of the lift force is calculated with MATLAB's Fast Fourier Transform (FFT) algorithm and plotted in figure 3-11. The lift force exhibits a distinct peak in all experiments at a frequency of about 3 Hz or $\frac{fd}{u_\infty} = 0.208$, which is consistent with theory.

The frequency of vortex shedding is determined by the width of the wake and the free stream velocity. The free stream velocity is the same for all experiments shown in figure 3-11, so the variation of the vortex shedding frequency is due to a variation in the wake width. Narrow wakes will roll up into vortices at a higher frequency than wide wakes. In this experiment, the the frequency of vortex shedding decreased with
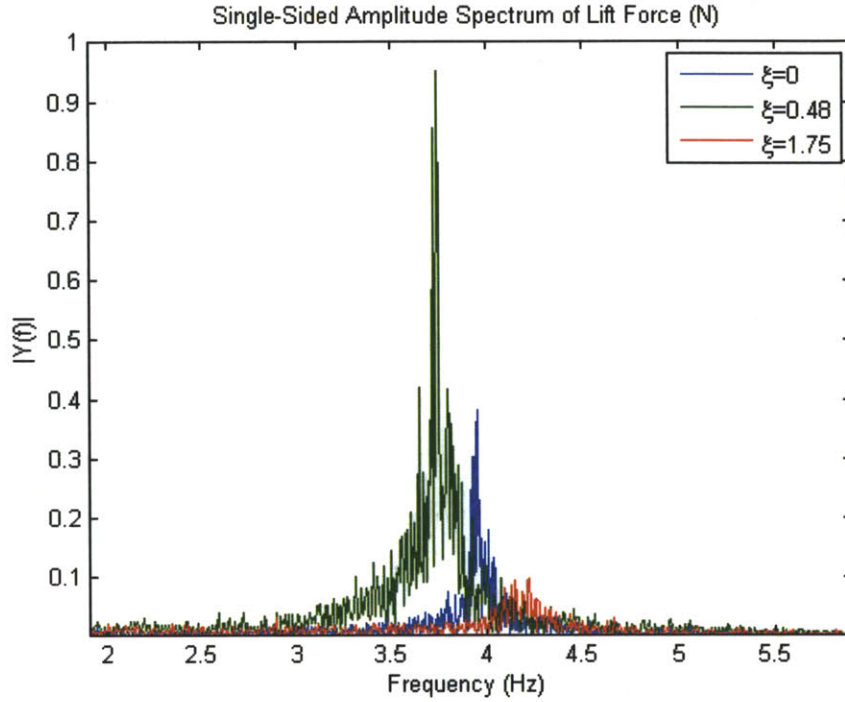
Figure 3-11: Spectra of the measured lift force.

respect to the baseline for $\xi < 1$ and increased with respect to the baseline for $\xi > 1$.
This result implies that the wake widened at low rotation rates and narrowed at high
rotation rates. And, since the mean drag varies directly with wake width, this result
is consistent with the mean drag measurements, which are shown in figure 3-10.

Additionally, the amplitude of the fluctuating lift force at the vortex shedding
frequency varies inversely with the vortex shedding frequency. That is, the reduction
in mean drag at high rotation rates is accompanied by an increase of the vortex
shedding frequency and a decrease of the amplitude of lift force fluctuations.

3.4   Flow Field Measurements

3.4.1   Mean Flow Field

The mean flow field illustrates the mean flow of momentum because water is incom-
pressible. The mean force that the fluid exerts on an object can be therefore be
calculated from the mean velocity field. A common strategy for mean drag calcula-
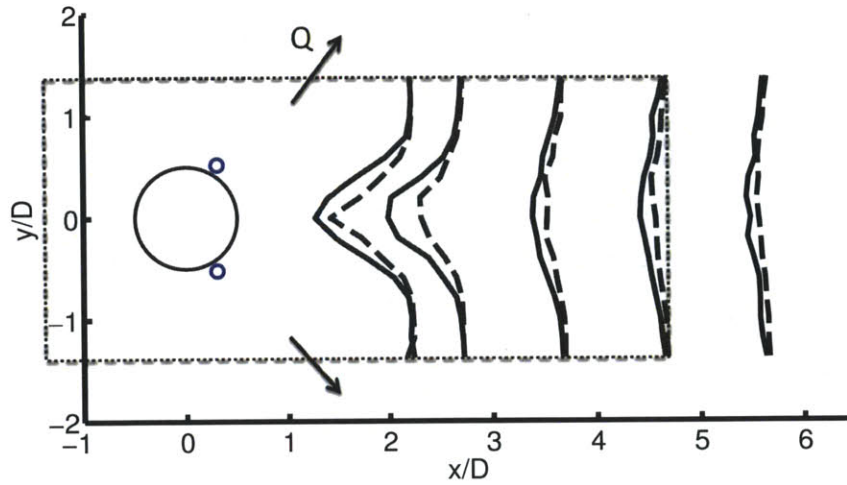
Figure 3-12: Mean stream-wise velocity profiles with a control volume (dotted line rectangle) enclosing the cylinder. The solid velocity profiles were measured when the rotation parameter, ξ, was 0, and the dotted profiles were measured when $\xi = 2.05$.

tion in water and wind tunnel experiments is to first draw a control volume around the model as in figure 3-12 [13]. In steady-state situations like this one, the mean drag force is equal to the transport of stream-wise momentum across the boundaries of the control volume.

$$D = \int_{CS} \rho \vec{v} (\vec{v} \cdot d\vec{A})$$

The velocity along the top and bottom sides of the control volume is approximately equal to the free stream value, u_∞, as shown in 3-12. However the mass flux across these sides, Q, is non-zero and calculated by taking the difference in mass flux across the upstream and down stream sides. The momentum flux across the top and bottom boundaries can be estimated as the product of mass flux, Q, and the free stream velocity, u_∞. The drag on the cylinder can thus be expressed as a function of the stream-wise velocity profile at a suitable station in the wake.

39

$$D = \rho \int_{-1.5\frac{y}{D}}^{1.5\frac{y}{D}} u|_{\frac{x}{D}=5}(u_{\infty} - u|_{\frac{x}{D}=5})dy$$

Drag results in a deficit of momentum in the wake. The reduction of drag by rotating cylinder flow separation control is immediately visible in figure 3-12 in the reduction of the wake momentum deficit. The mean drag coefficient calculated in this way from the mean flow field is plotted with the strain gauge measurements for comparison in figure 3-13. The large discrepancy between the two techniques for measuring drag is due two main differences. First, the control volume analysis calculates the drag on the entire system while the strain gauge only measured drag on the main cylinder. The difference is therefore partially due to the drag on the control cylinders. This might explain why the drag is underestimated at high rotation parameters where vortex shedding and so drag on the control cylinders is significantly reduced compared to the zero and low rotation rate cases. Second, the strain gauge measured the total force on the three-dimensional cylinder while the mean flow field was measured at one horizontal slice. The test section walls likely affected mean flow near the ends of the cylinder, which might result in variation of the mean flow field along the axial direction that the is not captured by measuring the mean flow field in a single slice.

3.4.2 Fluctuating Flow Field

The RMS flow field provides a measure of velocity fluctuations. Flow fluctuations are due to vortex shedding and turbulence. In the flow past a circular cylinder at moderate sub-critical Reynolds numbers like that of this experiment, velocity fluctuations are dominated by instabilities that result in vortices as opposed to turbulence. Large areas of strongly fluctuating fluid therefore indicate large and strong vortices. Contours of the root-mean-square transverse velocity field are plotted in figure 3-14.

The top plot in figure 3-14 shows the baseline case of flow past a circular cylinder with control cylinders located in the near wake but not rotating. The RMS flow

40
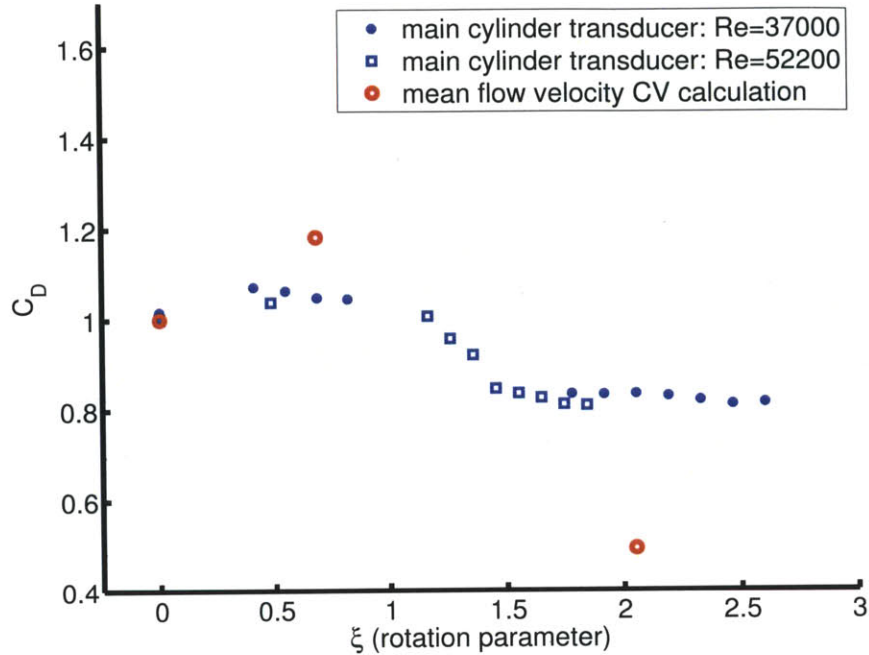
Figure 3-13: Mean drag coefficient measured with strain gauge and mean flow field.

field is very similar to the flow past a single circular cylinder. When the control cylinders rotate at a low rotation rate in the second image with $\xi = 0.68$, the area and shape of fluctuating flow changes slightly, but the amplitude of fluctuations remains unchanged. In particular, rotating the cylinders at the low rotation parameter brings strongly fluctuating flow closer to the cylinder. In the bottom plot in figure 3-14, the high rotation rate of the control cylinders of $\xi = 2.05$ significantly alters the flow. The area of fluctuating flow narrows and the amplitude of fluctuations is halved. Rotating the control cylinders at this rotation rate therefore reduces the size and strength of vortices shed from the main cylinder, which narrows the wake. This result is consistent with the reductions in mean drag and lift fluctuations measured with the force transducer and discussed in section 3.4.1.
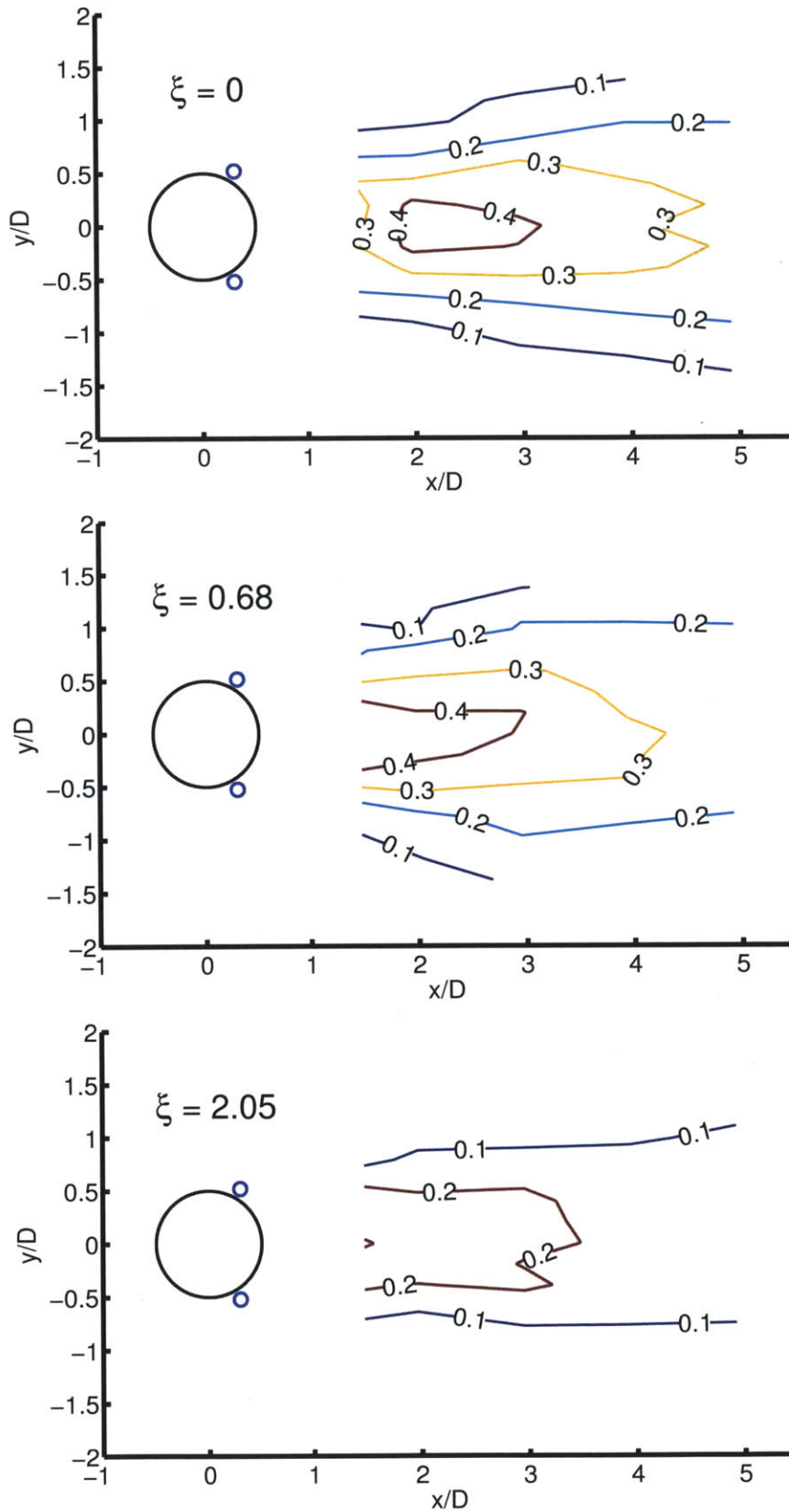
Figure 3-14: Contours of $\frac{v_{RMS}}{u_\infty}$ for different rotation rates. Flow is from left to right.

Chapter 4

Computational Simulations

4.1 Experiment Setup

4.1.1 Lily Pad Code

Computational experiments were conducted with the open source software, Lily Pad. Lily Pad is a two-dimensional solver written in Processing and designed for real-time fluid/structure interaction simulations. Algorithms are based on BDIM (Boundary Data Immersion Method) Cartesian-grid methods [20].

The flow past a circular cylinder at Reynolds numbers greater than 40 exhibits a strong instability mode known as the von Karman vortex street. As the Reynolds number increases greater than 2,000, higher mode instabilities arise in the wake. Three-dimensionality accompanies these higher mode instabilities [21]. A two-dimensional solver, therefore, cannot accurately calculate the flow in the physical experiments that were conducted at Reynolds numbers greater than 30,000. The two-dimensional solver does, however, have vastly increased computational speed as compared to three-dimensional solvers and still yields quantitatively similar results to the experimental findings discussed in this thesis.

4.1.2 Computational Domain

The computational domain must be sufficiently large to capture the important features of the flow. The computational domain for these simulations is 10 x 4 diameters, with the cylinder centered at 20% of the stream-wise dimension and 50% of the transverse length as shown in figure 4-1.
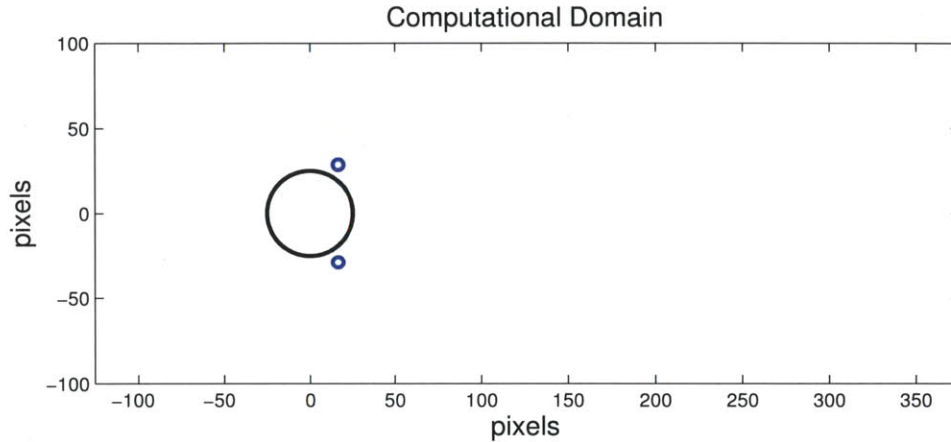
Figure 4-1: Computational domain: the flow is from left to right.

The resolution of the grid within this domain must be fine enough to capture the smallest relevant length scales. In this experiment, the smallest length scale is the gap between the main and control cylinders. Although the gap width was 2.5% of the main cylinder diameter in the physical experiments, the gap width was set to 10% of the main cylinder diameter in order to decrease computation time by allowing a coarser grid. The resolution was set to 50 grid points per main cylinder diameter, which corresponds to five grid points across the gap. The computational grid in the vicinity of the control cylinders is shown in figure 4-2 .

4.1.3 Drag Calculation

The force on the main cylinder is calculated by integrating the pressure around its circumference. Shear forces are not included in the calculation because they are assumed to be two orders of magnitude smaller than pressure forces [13]. Only the force on the main cylinder is included so that the calculated drag coefficients can be
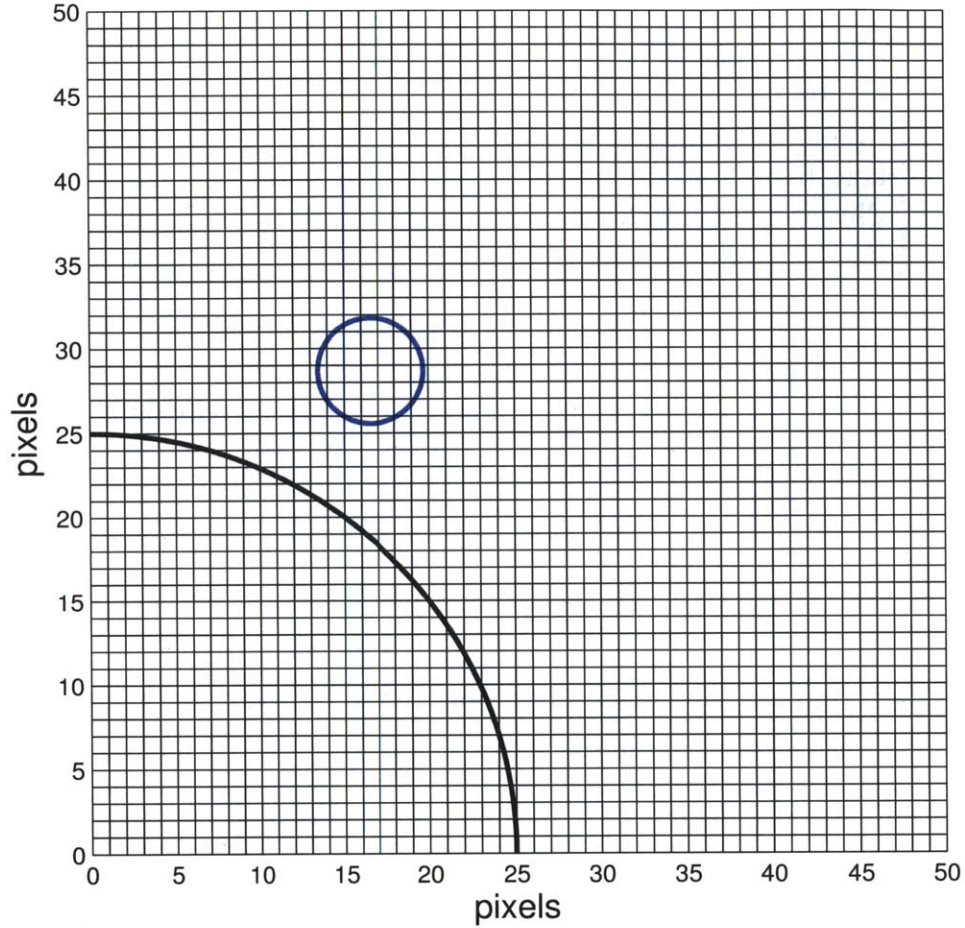
Figure 4-2: Cartesian grid in the vicinity of a control cylinder. There are 5 grid points spanning the gap between the main and control cylinders.

directly compared to those measured in the physical experiment, in which only the main cylinder was fixed to a force transducer.

4.1.4 Experiment Description

Vortex control with rotating cylinders is modeled by prescribing a velocity boundary condition at the surface of the control cylinders to be equal to the surface speed of a rotating cylinder. Each simulation is started with a rotation rate of zero for $tU/D < 50$. This period allows transients to die out and the von Karman vortex street mode to reach a limit cycle. The rotation parameter is then ramped at a rate of $0.005/(tU/D)$ until it reaches 2.0. This ramp rate is slow enough that the flow is

	Re_D	$\frac{d}{D}$	Re_d	$\frac{g}{D}$	ξ	θ
Computational, low Re	100	0.125	12.5	0.1	< 2	120°
Computational, high Re	10,000	0.125	1,250	0.1	< 2	120°
Physical, high Re	52,000	0.125	6,500	0.025	< 2	120°

Table 4.1: Summary of experiment parameters.

always in equilibrium. The rotation parameter increases by only 0.025 over a typical period of vortex shedding ($tU/D \approx 5$).

4.2   Simulations at $Re_D = 100$ ($Re_d = 12.5$)

The wake for $Re_D = 100$ exhibits the von Karman vortex street instability mode without any other instability modes. When the small control cylinders are introduced but not rotated, the wake is nearly unchanged. At $Re_d = 12.5$, vortices do not shed from the control cylinders, which instead have attached recirculation zones [21].

At zero control effort, the lift oscillates about a zero mean and the drag oscillates about a mean of 0.95. As the rotation parameter increases to 2.0 the mean drag and the amplitude of lift and drag fluctuations decrease linearly as shown in Figure 4-3 .
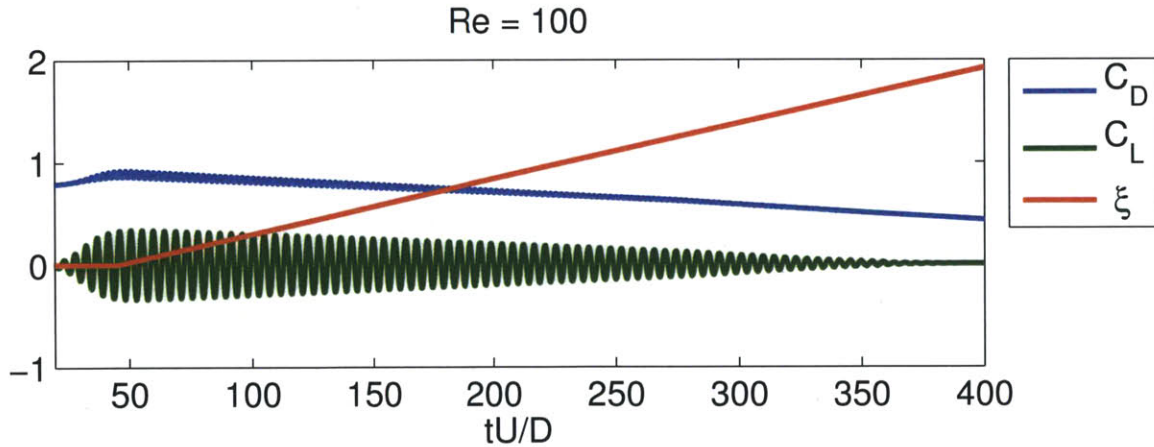

Figure 4-3: Computational simulations at Re = 100 show the pressure drag to decrease linearly with rotation parameter, ξ.

46

4.3 Simulations at $Re_D = 10{,}000$ ($Re_d = 1{,}250$)

The flow past a circular cylinder at $Re_D = 10{,}000$ exhibits higher mode instabilities as compared to the flow at $Re_D = 100$. When the small control cylinders are introduced to the flow, vortices shed from the small control cylinders in addition to the main cylinder beacuse $Re_d = 1{,}250$ is greater than 40, the Reynolds number at which vortices begin shedding from circular cylinders. This is shown in visualizations of the instantaneous vorticity field in figure 4-4.

As the rotation parameter increases from 0 to 1.0, vortex shedding from both the control cylinders and the main cylinder is apparent in the instantaneous vorticity field. As the rotation rate increases greater than 1.0, vortex shedding from the control cylinders diminishes until only the von Karman vortex street mode is present when the rotation parameter is 2.0.

The drag and lift remain nearly unchanged for rotation parameters between 0.0 and 1.0. The mean drag and amplitude of drag and lift fluctuations decreases for rotation parameter greater than 1.0. This result suggests that the presence of the control cylinder vortex shedding mode inhibits the efficacy of rotating cylinder control. And, when control cylinder vortex shedding is suppressed by rotation at $\xi > 1.0$, the rotating cylinders are able to effectively delay separation and reduce drag. This Reynolds number dependence of the mean drag vs. rotation parameter is shown in figure 5-4.
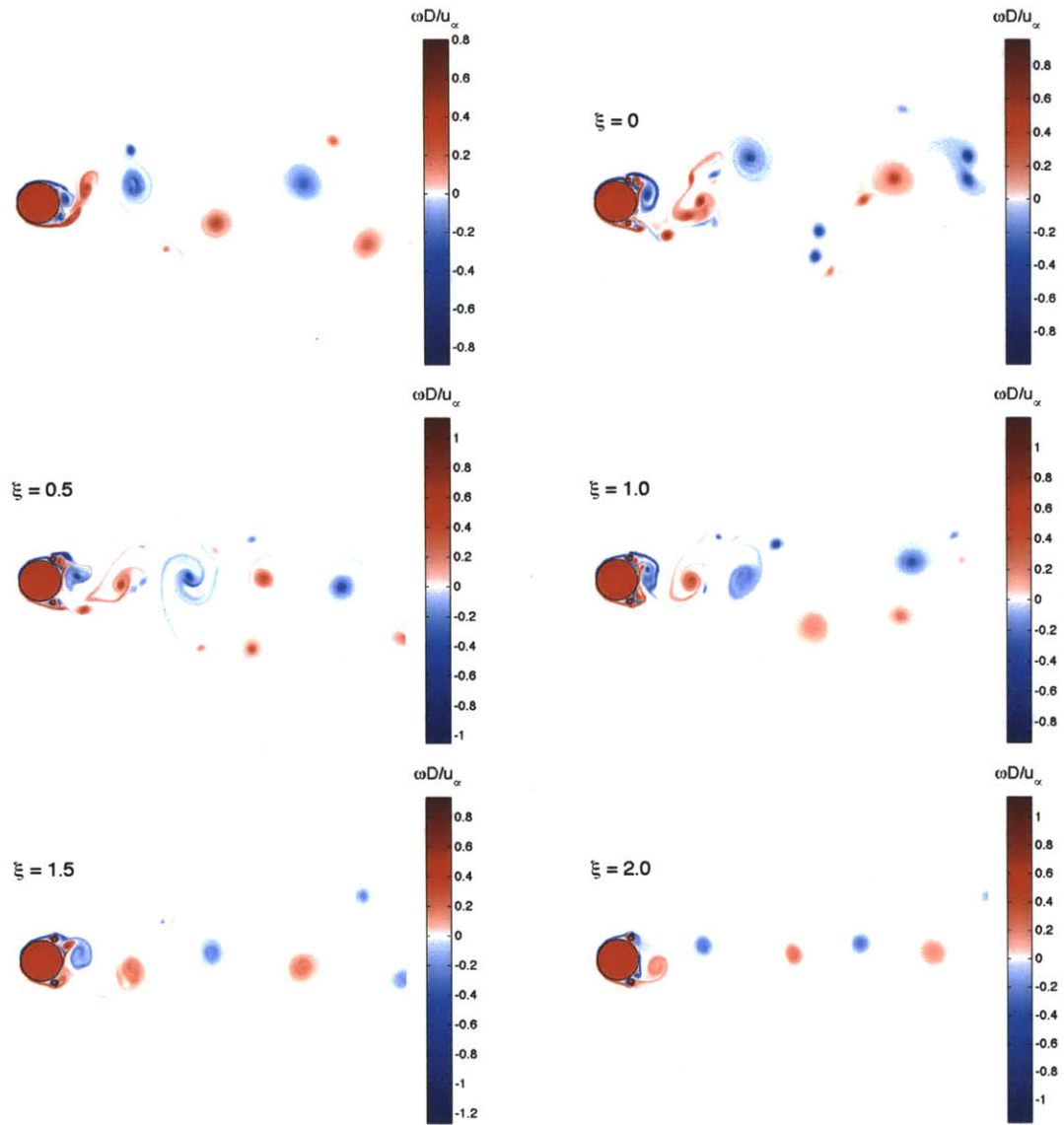
Figure 4-4: Visualizations of instantaneous vorticity field at Re = 10,000 for different rotation parameters, ξ.
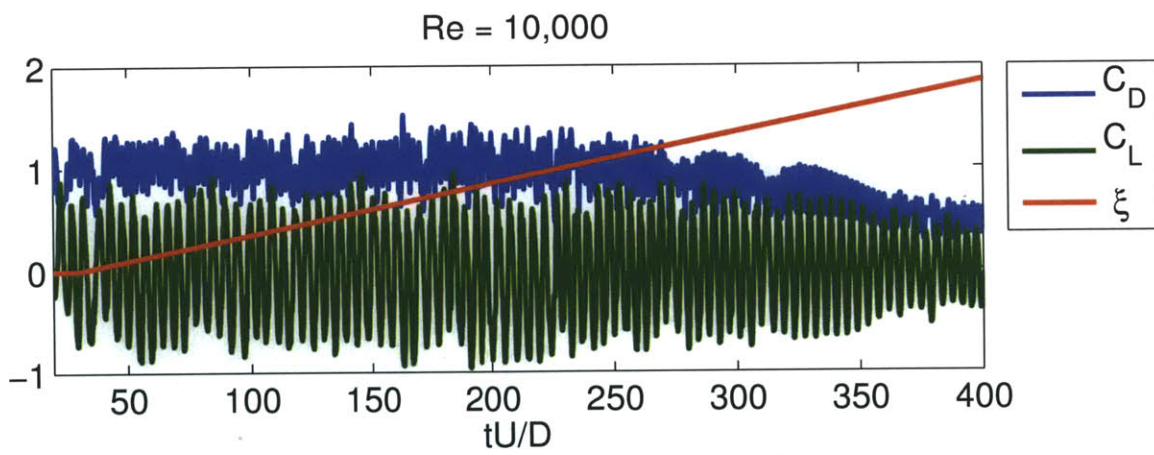
Figure 4-5: Computational simulations at Re = 10,000 show the pressure drag to decrease for rotation parameter $\xi > 1$.

Chapter 5

Discussion

5.1 Comparison of Simulated and Experimental Results

The physical and computational experiments have differences that require careful consideration. The most important of these involve the geometry and three-dimensionality. Despite these differences, the two experiments have quantitatively and qualitatively similar results. This suggests that the differences between the experiments do not negate the value of the simulation to better understand and illustrate the physical experiment.

First, the geometry of the two experiments is slightly different. The gap between the main and control cylinders, normalized by the main cylinder diameter, is four times greater in the computational than physical experiment. The physical experiment was designed first with as small a gap as possible. The computational experiment was conducted in Lily Pad, which, in its current form, is not flexible to variable density grids. As a result, resolving the flow with several grid points spanning the gap required a uniformly dense grid across the computational domain. Duplicating the geometry of the physical experiment had unfeasibly long computation time. Quadrupling the gap width is a relatively small change to the overall geometry because the gap is in both cases 10% of the main cylinder diameter or less. It was

estimated that this change in gap width would not significantly alter the global flow and, in particular, the drag force on the main cylinder. And, since quadrupling the gap width permitted the use of a coarser grid with much improved computation time, it was selected for this investigation.

The second important difference is that the simulation is two-dimensional while physical experiments cannot escape being three-dimensional. This is particularly important for three-dimensional cylinders with finite ends. In this experiment, the effects of finite ends were mitigated in the experimental setup as described in section 3.2.1. Additionally, flow instabilities of greater frequency and smaller length scale than the von Karman vortex street emerge at Reynolds numbers greater than 2,000 [21]. These higher-order instabilities introduce three-dimensional flow structures even for very long cylinders far away from finite ends, which a two-dimensional solver cannot capture.

Despite these differences, the drag reduction with rotation parameter is very similar in both the physical and simulated experiment, as shown in figure 5-1. The right image in figure 5-1 includes error bars that represent the standard deviation of the measured mean drag. The simulated drag coefficient lies within the error of the water tunnel measurements.

5.2   Reynolds Number Effects

Flow features like separation and vortex separation are Reynolds number regime dependent. In this experiment, a significant difference in the relationship between drag reduction and rotation parameter was observed for Re = 100 and 10,000. Visualizations of the flow simulations and frequency decomposition of the measured drag in the physical experiment together indicate that vortex shedding from the control cylinders is the source of the discrepancy between the drag reduction at Re = 100 and 10,000.

In the sub-critical Reynolds number range, an important regime shift occurs at approximately $Re_D = 40$, which marks the onset of vortex shedding that forms the
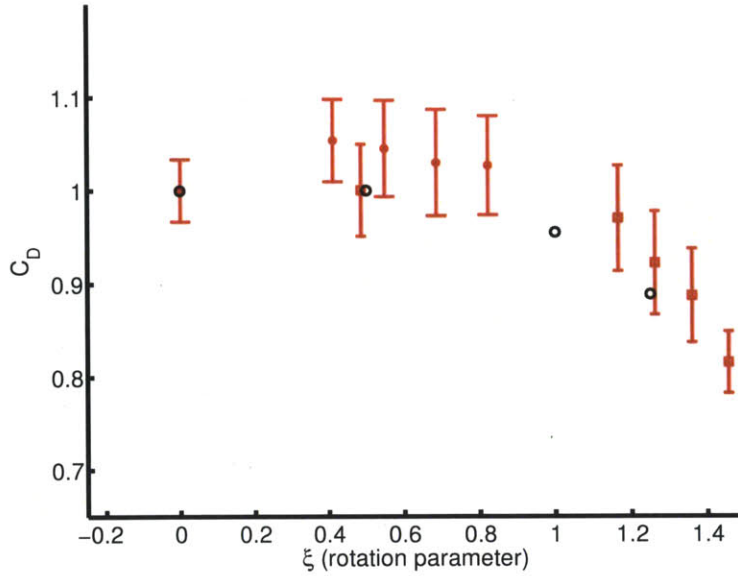
52

Figure 5-1: Mean pressure drag coefficient vs. rotation parameter as calculated in computational simulation (black open circles) and measured in water tunnel experiment (red filled circles with error bars). The calculation of error bars for the water tunnel results is discussed in section 3.3.

von-Karman vortex street in the wake [21]. The geometry under consideration in this thesis has two characteristic lengths, which are the diameters of the main and control cylinders. A Reynolds number can be calculated with each: $Re_D = \frac{Du_\infty}{\nu}, Re_d = \frac{d}{D}Re_D$. In this experiment, $Re_d = 12.5$ at the lower Reynolds number and 1,250 at the higher Reynolds number. As a result, vortex shedding can be expected from the main cylinder at both Reynolds numbers but from the control cylinders at only the higher Reynolds number. This is apparent in the instantaneous vorticity field calculated in the computational simulations and shown in figure 5-2. Only the von Karman vortex street mode is apparent in the Re = 100 flow while higher modes are visible in the Re = 10,000 flow.

The instantaneous vorticity field is plotted for the computational experiment at Re = 10,000 in Figure 4-4. When the rotation parameter is less than 1.0, vortex shedding from both the control cylinders and the main cylinder is apparent in the instantaneous vorticity field. When the rotation parameter is equal to 2.0, only vortex shedding from the main cylinder remains. That is, rotating the control cylinders at a rotation parameter greater than 1.0 eliminates vortex shedding from the control
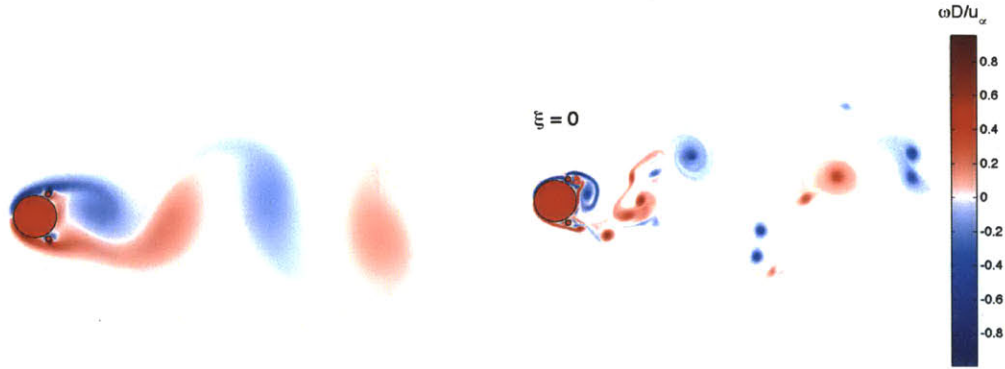
Figure 5-2: Visualizations of instantaneous vorticity field with stationary control cylinders ($\xi = 0$) at Re $= 100$ (left) and Re $= 10,000$ (right).

cylinders. This is consistent with observations of the suppression of vortex shedding from rotating cylinders in close proximity to a wall studied, albeit at lower Reynolds numbers, in [15]. The rotation rate at which vortex shedding is suppressed varies inversely with the gap width [5].

Vortex shedding from the control cylinders at low rotation rates was also observed indirectly in the water tunnel experiment. When the free stream was increased to 1.5m/s, at which velocity a Strouhal frequency of 0.2 approached the first vibration mode frequency of the control cylinders, the control cylinders were observed to vibrate with large amplitude. The large amplitude vibrations were likely caused by vortex shedding. This implies that vortices shed from the control cylinders when they are not rotated at a frequency on the order of St $= 0.2$, which is the frequency at which vortices shed from a circular cylinder in cross-flow in the Reynolds number regime of the experiment [21]. The experiments in rotating cylinder flow separation control were conducted at a reduced velocity to avoid large amplitude vortex-induced-vibrations (VIV).

The frequency spectra of the measured drag force was calculated with MATLAB's Fast Fourier Transform algorithm. The spectra for a selection of the experiments is plotted in figure 5-3. In the experiments with rotation parameter less than 1.2, there is a peak at control cylinder St $= 0.25$ in addition to peaks at the rotation rate and the frequency of vortex shedding from the main cylinder (about 3Hz). It
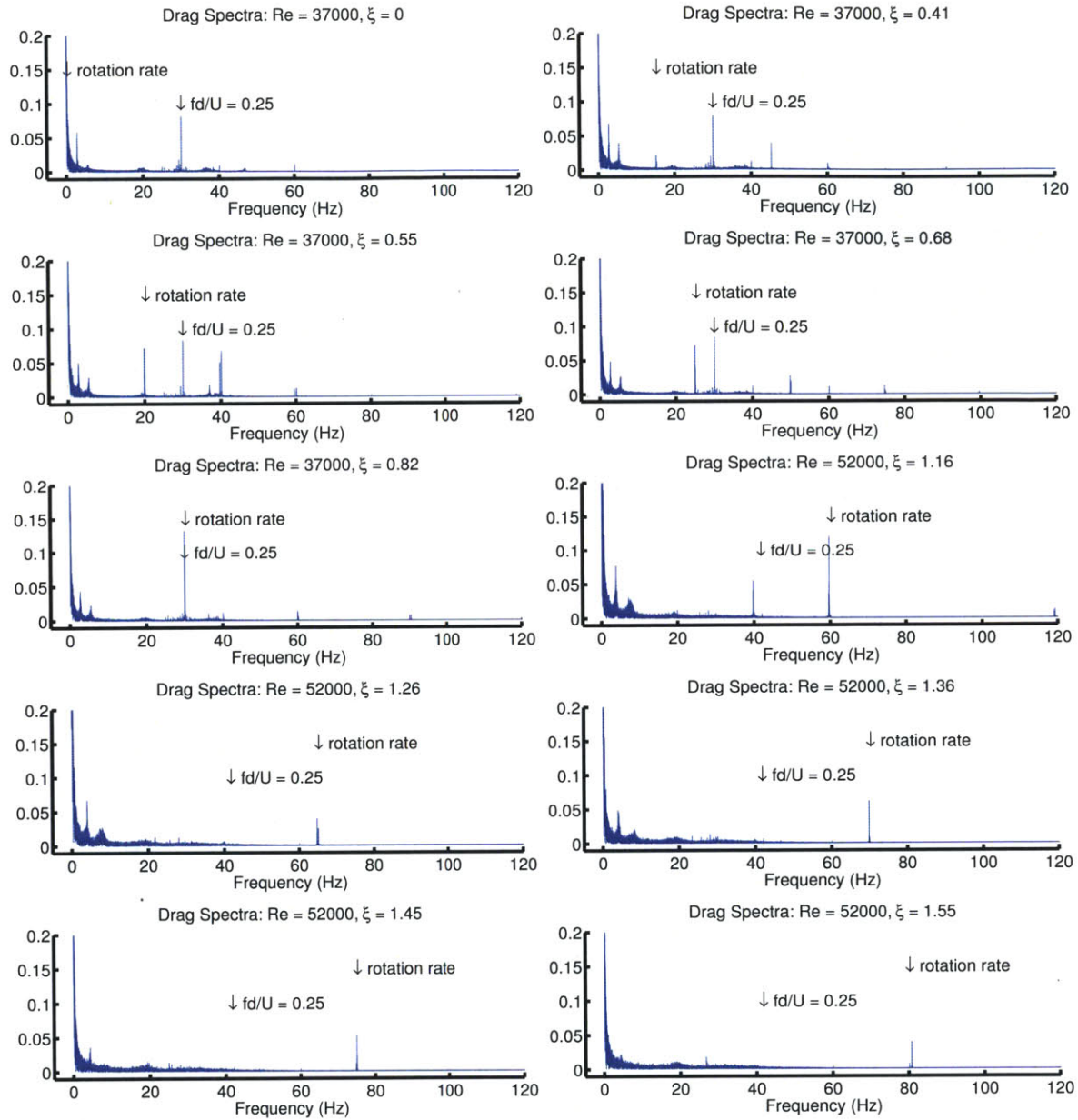
Figure 5-3: Frequency spectra of measured experiment drag calculated with MAT-LAB's FFT algorithm.

is likely that this peak corresponds to vortex shedding from the control cylinders because it is on the order of 0.2 and no other disturbances at that frequency were known or suspected. The vortex shedding frequency is far enough from the control cylinder natural frequency of 50 Hz (see section 3.2.3) that the control cylinders did not experience large amplitude VIV. However, the shed vortices likely created fluctuations in the drag of the main cylinder at the same frequency.

As the rotation parameter increases greater than 1.2, the peak in the drag spectra at the control cylinder vortex shedding frequency disappears, which suggests that vortex shedding from the control cylinders is suppressed by high rotation rates. This result is consistent with the visualizations of the instantaneous vorticity field in the computational experiment described in chapter 4.
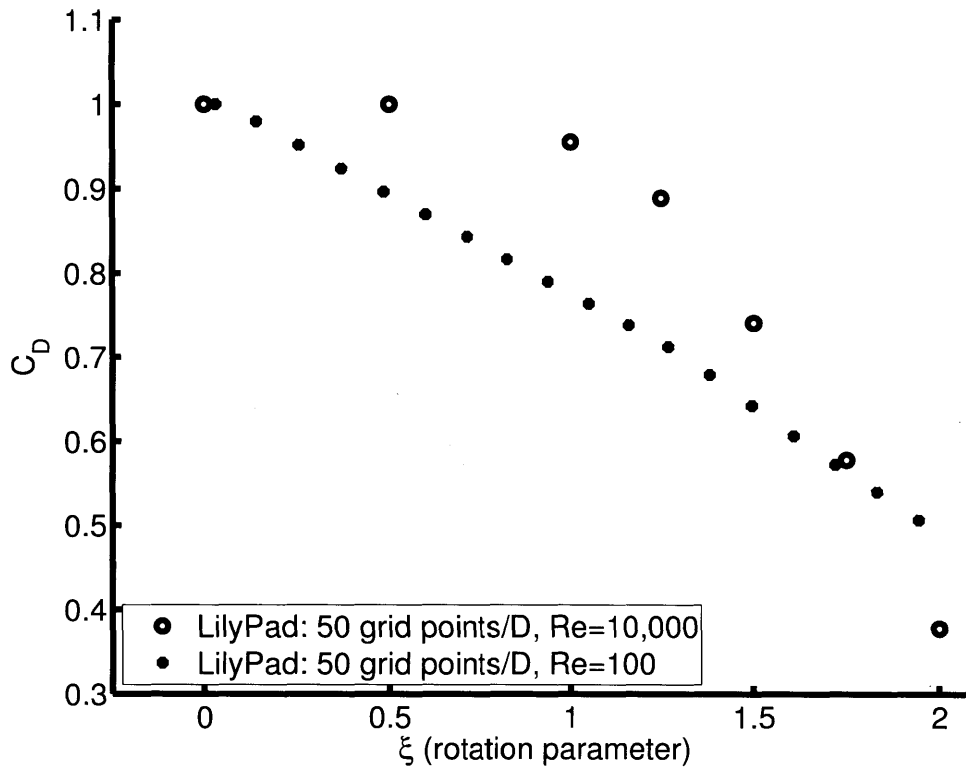
Figure 5-4: Mean pressure drag coefficient vs. rotation parameter as calculated in computational simulation at different Re = 100 and 10,000.

A consequence of this phenomenon is an altered relationship between drag reduction and rotation parameter, shown in figure 5-4. At low Reynolds numbers at which vortices do not shed from the control cylinders, the drag on the main cylinder reduces linearly with increasing rotation parameter. At higher Reynolds numbers at which vortices do shed from the control cylinder, the drag is insensitive to rotation parameters less than 1, which is the range of rotation rates for which vortices shed from the control cylinders. The drag decreases with increasing rotation rate for rotation parameters greater than 1, which is the range of rotation rates for which rotation suppresses vortex shedding from the control cylinders. One can tentatively conclude

from these results that vortex shedding from the control cylinders limits the efficacy of rotating cylinder flow separation control.

The phenomenon is observed only indirectly in the experimental results. Velocity measurements of the flow in the immediate wake of the small control cylinders would provide more convincing evidence of vortex shedding. Particle Image Velocimetry (PIV) would provide instantaneous data of the flow field in which vortices could be observed. LDA could also be used to sample the velocity at a single location in the near wake of a control cylinder at an even higher frequency than with PIV. The frequency spectra of this data would also convincingly indicate the presence of vortex shedding.

5.3 Power Consumption

Total power consumption includes the power to translate the body and to actuate any active flow control. An active separation control strategy is only useful if it reduces the total power consumption. Otherwise, the additional energy expenditure is more efficiently applied to greater propulsion force than reducing resistance. The non-dimensional power consumption, P^* is the power consumption normalized by its value at zero control effort. Values of P^* less than one indicate a net benefit to using active control.

$$P^*(\xi) = \frac{P(\xi)_{trans} + P(\xi)_{control}}{P_{trans}|_{\xi=0}}$$

The translational power is equal to the product of the drag force and velocity, which can be expressed in terms of the drag coefficient. Note that this expression for power does not include power loss outside of the fluid. For example, power loss in an engine or in the transmission of power between the engine and propulsor are not included.

$$P_{trans} = \frac{1}{2}\rho D L u_\infty^3 C_D$$

Only shear stress and no normal stress resists the rotation of a circular cylinder in a fluid. The shear stress is proportional to the velocity gradient at the surface of the control cylinder. The velocity gradient in this experiment at the boundary of the control cylinders varies in both time and space. However, a conservative estimate for the mean resistance to rotation can be made by using the friction coefficient for flow over a flat plate. An appropriate characteristic velocity is the speed of the surface of the control cylinder. Using the surface speed of the cylinder overestimates the resistance because the actual change in velocity across the boundary layer will be less. The power consumed by rotating two control cylinders is therefore conservatively estimated as:

$$P_{control} = \rho \pi d L u_{surface}^3 C_f$$

The total power consumption for a system with two control cylinders can now be expressed as a function of drag coefficients, diameters, and the rotation parameter, ξ.

$$P^* = \frac{C_D(\xi)}{C_D|_{\xi=0}} + 2\pi \frac{C_f}{C_D|_{\xi=0}} \frac{d}{D} \xi^3$$

The first of these terms is on the order of 50%, as is shown in Figure 5-4. The second of these is on the order of 1%. The ratio of the friction coefficient to the drag coefficient is less than 1% and the significant drag reductions found in this investigation were accomplished at $\frac{d}{D}\xi^3 < 1$. This implementation of rotating cylinder flow control therefore reduces the total power transfered to the fluid to translate a two-dimensional circular cylinder. In fact, Beaudoin et al calculate a power cost function associated with rotating cylinder flow separation control that disregards hydrodynamic power loss entirely because it is "negligible" [2].

Chapter 6

Conclusion

A flow separation control mechanism comprised of two counter-rotating cylinders placed in close proximity to a main cylinder has been shown to successfully reduce the mean drag on a circular cylinder in cross-flow by up to 20% in physical experiments at Re = 52,000. The relationship between drag and rotation parameter was discovered to be non-linear at this Reynolds number, which is a significant divergence from the the relationship at flows with Reynolds number on the order of 100. The presence of vortex shedding from the control cylinders at low rotation rates desensitizes the drag to the control mechanism. However, as the rotation parameter increases greater than 1.0, rotation suppresses vortex shedding from the control cylinders and significant drag reduction is realized. Finally, the power consumption of this active mechanism is estimated to be an order of magnitude less than the power savings in drag reduction.

Future work should include the investigation of the performance of other geometric parameters. In this thesis, a single geometry was considered and small improvements in drag reduction might result from tweaking the parameters, including the location and size of the rotating control cylinders. This thesis also only considers a steady rotation rate, but oscillating the rotation rate of the cylinders both in and out of phase with each other and at frequencies near or far from the vortex shedding frequency could have interesting results. Future work should also investigate close-loop feedback control of the rotation rate of the cylinders. Feedback could come from the force transducer or even more direct measurements of the flow such as pressure and velocity

sensors.

The most important and also most difficult future task will be the transition from the flow past a two-dimensional circular cylinder to active flow separation control on maneuvering three-dimensional ocean vehicle shapes. The three-dimensional helical vortex separation of such flows introduces significant complexity to all aspects of active flow separation control.

Bibliography

[1] H. M. Badr, M. Coutanceau, S. C. R. Dennis, and C. Mnard. Unsteady flow past a rotating circular cylinder at reynolds numbers 10 3 and 10 4. *Journal of Fluid Mechanics*, 220(-1):459, April 2006.

[2] Jean-Francois Beaudoin, Olivier Cadot, Jean-Luc Aider, and Jose-Eduardo Wesfreid. Drag reduction of a bluff body using adaptive control methods. *Physics of Fluids*, 18(8):085107, 2006.

[3] J.F. Beaudoin, O. Cadot, J.L. Aider, and J.E. Wesfreid. Bluff-body drag reduction by extremum-seeking control. *Journal of Fluids and Structures*, 22(6-7):973–978, August 2006.

[4] Richard G Budynas, J. Keith Nisbett, and Joseph Edward Shigley. *Shigley's mechanical engineering design*. McGraw-Hill, Boston, 2008.

[5] Ming Cheng and Li-Shi Luo. Characteristics of two-dimensional flow around a rotating circular cylinder near a plane wall. *Physics of Fluids*, 19(6):063601, 2007.

[6] Haecheon Choi, Woo-Pyung Jeon, and Jinsung Kim. Control of flow over a bluff body. *Annual Review of Fluid Mechanics*, 40(1):113–139, January 2008.

[7] Taeyoung Han and V.C. Patel. Flow separation on a spheroid at incidence. *Journal of Fluid Mechanics*, 92(4):643–657, July 1978.

[8] C. Homescu, I. M. Navon, and Z. Li. Suppression of vortex shedding for flow around a circular cylinder using optimal control. *International Journal for Numerical Methods in Fluids*, 38(1):43–69, January 2002.

[9] C Kuo, L Chiou, and C Chen. Wake flow pattern modified by small control cylinders at low reynolds number. *Journal of Fluids and Structures*, 23(6):938–956, August 2007.

[10] S Mittal. CONTROL OF FLOW PAST BLUFF BODIES USING ROTATING CONTROL CYLINDERS. *Journal of Fluids and Structures*, 15(2):291–326, February 2001.

[11] V Modi. MOVING SURFACE BOUNDARY-LAYER CONTROL: a REVIEW. *Journal of Fluids and Structures*, 11(6):627–663, August 1997.

[12] Sridhar Muddada and B.S.V. Patnaik. An active flow control strategy for the suppression of vortex structures behind a circular cylinder. *European Journal of Mechanics - B/Fluids*, 29(2):93–104, March 2010.

[13] J. N Newman. *Marine hydrodynamics*. MIT Press, Cambridge, Mass., 1977.

[14] B. Patnaik and G. Wei. Controlling wake turbulence. *Physical Review Letters*, 88(5), January 2002.

[15] A. Rao, B.E. Stewart, M.C. Thompson, T. Leweke, and K. Hourigan. Flows past rotating cylinders next to a wall. *Journal of Fluids and Structures*, 27(5-6):668–679, July 2011.

[16] A. Richter and E. Naudascher. Fluctuating forces on a rigid circular cylinder in confined flow. *Journal of Fluid Mechanics*, 78:561–576, 1976.

[17] S. Szepessy and P. W. Bearman. Aspect ratio and end plate effects on vortex shedding from a circular cylinder. *Journal of Fluid Mechanics*, 234:191–217, 1992.

[18] Oskar Gustav Tietjens, Ludwig Prandtl, and Louis Rosenhead. *Fundamentals of hydro- and aeromechanics based on lectures of L. Prandtl*. Dover Publications, New York, 1957.

[19] G. S. West and C. J. Apelt. The effects of tunnel blockage and spect ratio on the mean flow past a circular cylinder with reynolds numbers between 10^4 and 10^5. *Journal of Fluid Mechanics*, 114:361–377, 1982.

[20] G.D. Weymouth and Dick K.P. Yue. Boundary data immersion method for cartesian-grid simulations of fluid-body interaction problems. *Journal of Computational Physics*, 230(16):6233–6247, July 2011.

[21] M. M Zdravkovich. *Flow Around Circular Cylinders Volume 1: Fundamentals*. Univ. Press, Oxford [u.a.], 1997.

[22] M. M. Zdravkovich. *Flow around circular cylinders : a comprehensive guide through flow phenomena, experiments, applications, mathematical models, and computer simulations. Vol. 2, [Applications]*. Oxford University Press, Oxford, 2003.